

This preprint has been submitted to a peer-reviewed journal.

Submission date: 3 February 2025.

Robust blue-green urban flood risk management optimised with a genetic algorithm for multiple rainstorm return periods

Asid Ur Rehman ^{1*}, Vassilis Glenis ¹, Elizabeth Lewis ², Chris Kilsby ¹, Claire Walsh ¹

¹ School of Engineering, Newcastle University, Newcastle Upon Tyne, NE1 7RU, UK

² School of Engineering, The University of Manchester, Manchester, M1 7HL, UK

* Correspondence: asid-ur-rehman2@newcastle.ac.uk

Abstract

Flood risk managers seek to optimise Blue-Green Infrastructure (BGI) designs to maximise return on investment. Current systems often use optimisation algorithms and detailed flood models to maximise benefit-cost ratios for single rainstorm return periods. However, these schemes may lack robustness in mitigating flood risks across different storm magnitudes. For example, a BGI scheme optimised for a 100-year return period may differ from one optimised for a 10-year return period. This study introduces a novel methodology incorporating five return periods ($T = 10, 20, 30, 50,$ and 100 years) into a multi-objective BGI optimisation framework. The framework combines a Non-dominated Sorting Genetic Algorithm II (NSGA-II) with a fully distributed hydrodynamic model to optimise the spatial placement and combined size of BGI features. For the first time, direct damage cost (DDC) and expected annual damage (EAD), calculated for various building types, are used as risk objective functions, transforming a many-objective problem into a multi-objective one. Performance metrics such as Median Risk Difference (MedRD), Maximum Risk Difference (MaxRD), and Area Under Pareto Front (AUPF) reveal that a 100-year optimised BGI design performs poorly when evaluated for other return periods, particularly shorter ones. In contrast, a BGI design optimised using composite return periods enhances performance metrics across all return periods, with the greatest improvements observed in MedRD (22%) and AUPF (73%) for the 20-year return period, and MaxRD (23%) for the 50-year return period. Furthermore, climate uplift

stress testing confirms the robustness of the proposed design to future rainfall extremes. This study advocates a paradigm shift in flood risk management, moving from single maximum to multiple rainstorm return period-based designs to enhance resilience and adaptability to future climate extremes.

Keywords

multi-objective optimisation; genetic algorithm; blue-green infrastructure; multiple return periods; robust flood risk management; climate change resilience

1 Introduction

Flooding, a prevalent global natural disaster, exposes 1.47 billion people to 1-in-100-year risk, with annual losses rising from \$6 billion in 2005 to an expected \$60 billion by 2050 (Salhab & Rentschler, 2020). As urbanisation expands (Miller & Hutchins, 2017; Rentschler et al., 2023) and climate change intensifies, flood events are becoming more frequent and severe (Kendon et al., 2023; Robinson et al., 2021). Traditional urban flood risk management (FRM) approaches, primarily relying on subsurface drainage, designed by historical rainfall data, often struggle to handle extreme and varying rainfall patterns, leaving cities at unprecedented risk (Salinas-Rodriguez et al., 2018). This escalating risk to cities highlights the need for innovative and robust FRM designs to tackle the adverse impact of rainstorm events of varying intensities.

Grey Infrastructure (GI), such as drainage systems and concrete barriers, manages runoff but often fails during severe rainstorms due to limited capacity (D'Ambrosio et al., 2022; Salinas-Rodriguez et al., 2018). Expanding GI can increase capacity, but it is costly, unsustainable, impractical in dense urban areas, and potentially degrades ecosystems (Qin et al., 2013; Rosenbloom, 2018). Such limitations highlight the need for sustainable alternatives such as Blue-Green Infrastructure (BGI) or Low Impact Development (LID). These approaches use semi-natural features such as permeable surfaces, green roofs, rain gardens, and detention/retention ponds to enhance flood risk management by integrating natural hydrological processes like infiltration, evaporation, and temporary storage into urban planning (Alves et al., 2019; O'Donnell et al., 2020; Webber et al., 2020). Beyond managing floods, BGI proves beneficial in boosting biodiversity, mitigating heat islands, and improving urban environments (Ahiablame et al., 2012; Rodriguez et al., 2021). The adaptability, sustainability, and multifunctionality of BGI make it ideal

for retrofitting flood management systems by complementing traditional GI methods and driving policy shifts in city councils towards 'blue-green' urban planning (Liberalesso et al., 2020; Manchester City Council, 2021; Wheeler, 2016).

Sustainable FRM requires efficient resource allocation and robust designs that perform across varying rainstorm intensities (Sharma et al., 2021). The literature suggests that the cost-effectiveness and robustness of BGI largely depend on the hydrodynamic models and risk assessment functions used to evaluate design parameters such as BGI type, location, and size. (Maier et al., 2019; Seyedashraf et al., 2021; Wang et al., 2022). For instance, semi-distributed models like the Storm Water Management Model (SWMM) (Rossman & others, 2010) evaluate BGI efficiency and robustness by considering reduced peak flows and water volumes in drainage networks (Zhi et al., 2022), barely addressing surface flooding and related risks, usually termed stormwater management. Fully distributed models such as CityCAT (Glenis et al., 2018; Iliadis et al., 2023) explicitly simulate BGI to assess its effectiveness in reducing surface runoffs and associated risks to buildings, properties, and infrastructure, providing a more accurate representation of surface FRM. The literature reports that most BGI designs for FRM, developed using detailed flood models, often rely on limited options evaluated through multi-criteria (Alves et al., 2018; Joshi et al., 2021) or scenario-based designs (Abduljaleel & Demissie, 2021; D'Ambrosio et al., 2022; Iliadis et al., 2024; Vercruyssen et al., 2019; Webber et al., 2020), which restrict BGI deployment options and may not ensure cost-effective designs. To address this challenge, a multi-objective optimisation algorithm is integrated with a fully distributed hydrodynamic flood model to systematically achieve the most cost-effective BGI design (Ur Rehman et al., 2024). In line with industry practice, a 100-year return period was initially used to optimise permeable surfaces' location and overall size. However, the 100-year design performed poorly when tried for a 30-year return period, possibly due to a discrete risk objective function, which only accounts for BGI performance in risk reduction when a certain threshold is met. The outcomes highlight the need to investigate BGI optimisation further using continuous risk functions across different return periods. A continuous risk objective should capture the full range of risk reduction, from very minor to maximum. Furthermore, a novel approach is needed to optimise multiple return periods

simultaneously, potentially leading to robust FRM. To the authors' knowledge, no such method has yet been developed or tested in multi-objective optimisation, highlighting a considerable research gap.

This study addresses the identified research gap by developing an FRM design that is both cost-effective and robust across varying rainstorm intensities. The study seeks to consider whether the current paradigm of FRM, usually based on a single maximum return period, should persist or be replaced by a more comprehensive approach. The novelty of this work lies in the simultaneous incorporation of multiple rainstorm return periods and the design of a continuous risk function for optimisation to develop a comprehensive blue-green FRM approach. The specific objectives of this study are to: (i) design a continuous risk objective function for optimisation and analyse subsequent optimisation results for distinct return periods, (ii) incorporate multiple return periods into a multi-objective optimisation framework to achieve a composite BGI design, (iii) quantitatively assess optimisation performance for individual and composite optimised BGI designs, (iv), calculate realistic cost-benefits for BGI lifespan and (v) conduct a stress test to evaluate the climate change resilience of the newly proposed FRM method. The rest of this paper is organised as follows: Section 2 covers the study area and detailed methodology; Section 3 presents the results and discussions, study limitations, and future recommendations. Lastly, section 4 provides the concluding remarks.

2 Material and methods

2.1 Study area

The study area, shown in Figure 1, is an urban catchment in Newcastle upon Tyne. The catchment has a total area of approximately 5.3 km², of which approximately 43% is green/permeable area, 32% is impervious surfaces, and 25% is buildings. Based on type, the building area is further classified into residential (10%) and non-residential (15%) categories. The catchment has a maximum elevation of 120 meters, with a relatively steep slope of 3.3% from northwest to southeast (see the elevation map in supplementary information S1). The high gradient allows rainstorm water to move relatively quickly from the upper catchment to the lower catchment, placing infrastructure and properties in the lower catchment at high risk.

Newcastle has experienced numerous flash floods due to heavy rainstorm events (Newcastle City Council, 2016), the most severe being 'Thunder Thursday,' during which the city received 49 mm of rainfall in 2 hours (Environmental Agency, 2012). This rainstorm was approximated as a 100-year return period event.

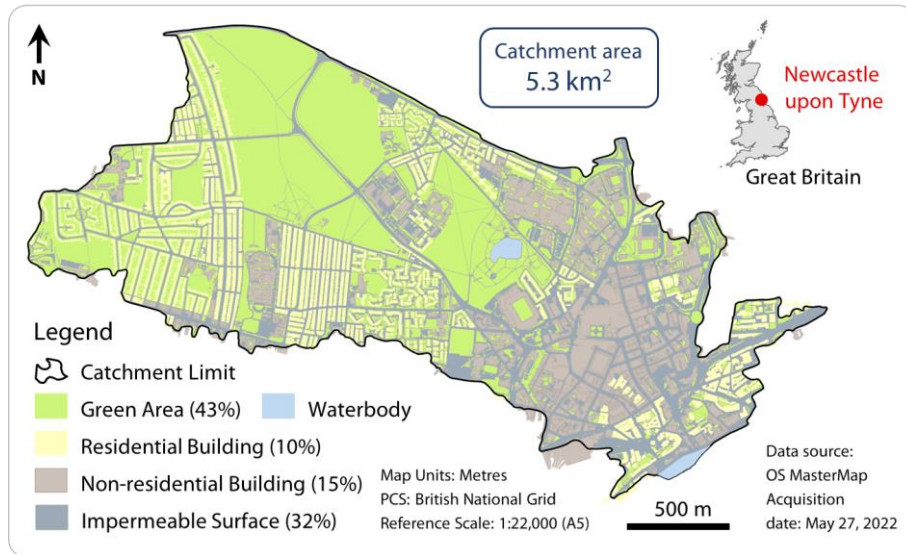


Figure 1. Map of the study area

2.2 Designing rainstorm events

The standard Depth-Duration-Frequency (DDF) model for the UK (Faulkner, 1999) was used to calculate the total rainfall amount for 100, 50, 30, 20, and 10-year return periods (T), each with a duration (t) of 30 minutes. The DDF model equation used for rainfall with a duration of 12 hours or less is given below:

$$\ln(R) = (cy + d_1) \ln(D) + ey + f \quad \text{where } y = -\ln \left[-\ln \left(1 - \frac{1}{T} \right) \right]$$

R is the rainfall depth, D is the duration, y is the Gumbel reduced variate, T is the return period, and c, d₁, e, f are catchment descriptors. The hyetograph generation method from the Flood Studies Report (FSR) (Institute of Hydrology, 1975) was then applied to generate temporal distribution profiles for the given rainfall events in an urban catchment. The equation to create the rainfall distribution profile is given below:

$$y = \frac{1 - a^z}{1 - a} \quad \text{where } z = x^b$$

Where: y is the fraction of the rainfall that drops within the proportion x of the total rainstorm duration. Parameters a and b have fixed values, and the profile is centred on the peak. The obtained rainfall totals

and temporal distributions for the considered return periods with the same durations are shown in Figure 2.

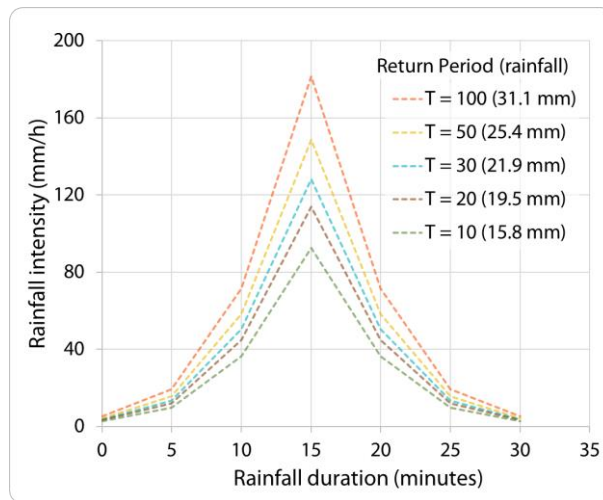


Figure 2. Design rainstorms for five return periods

2.3 Climate change uplift

A stress test using three climate change uplifts, classified as low, medium, and high, assessed the resilience of the proposed FRM design. Based on Chan et al. (2023), rainfall increases of 15%, 30%, and 45% were applied to baseline return periods for each uplift. Figure 3 shows how these uplifts can be considered equivalent to an increase in the return period. For example, a 45% rainfall increase for a 100-year storm equates to a 360-year return period on the baseline scale.

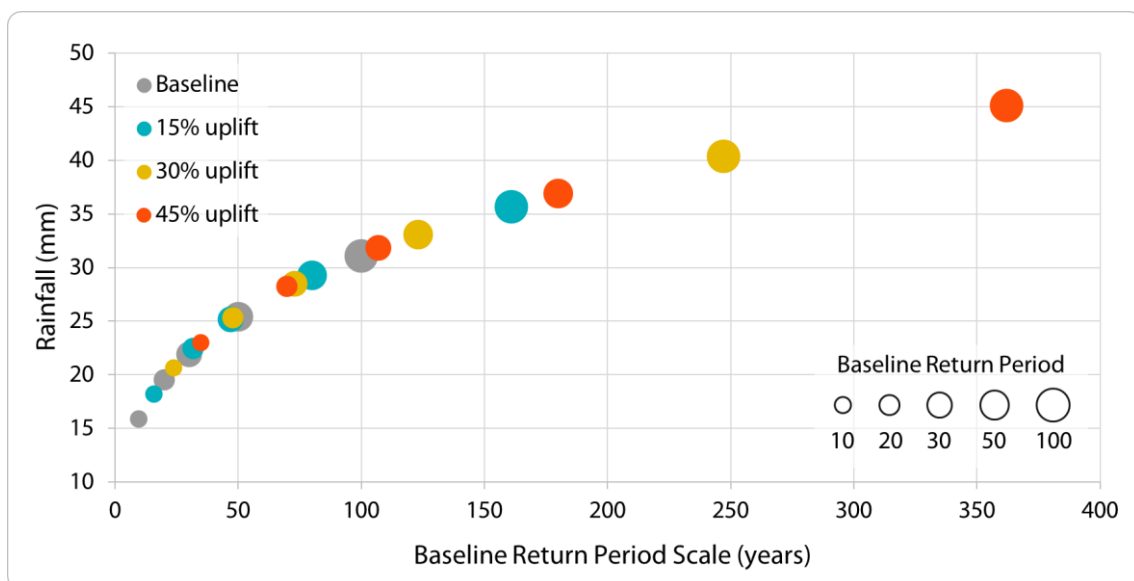


Figure 3. Different climate uplifts on baseline return periods

2.4 Hydrodynamic flood modelling

This study uses the advanced City Catchment Analysis Tool (CityCAT) (Glenis et al., 2018). CityCAT is a fully distributed, physically-based hydrodynamic model that uses a high spatial resolution Digital Elevation Model (DEM) to explicitly represent land use features, including buildings, permeable green spaces, and impervious areas. It also simulates the hydrodynamics of BGI, incorporating features such as permeable surfaces, green roofs, and water butts. Surface water elements like detention ponds and rivers are represented within the DEM. CityCAT takes rainfall, DEM, land use and BGI inputs and applies shallow water equations to simulate 2D water depths and velocities across the spatial domain. It can also integrate subsurface sewer networks to compute coupled surface-subsurface water flows and volumes, though this significantly increases computational time. Due to such computational constraints, this study only uses CityCAT's 2D surface flood simulation module. Further details on its role within the optimisation framework are provided in section 2.6.2. For a comprehensive overview of CityCAT, refer to Ur Rehman et al. (2024), with detailed information in Glenis et al. (2018).

2.5 Permeable surface intervention design

The current study builds on previous research (Ur Rehman et al., 2024), which assessed the cost-effectiveness of permeable surface interventions by dividing the entire catchment into zones of varying sizes and quantities. The best-performing scenario, featuring 80 permeable zones (shown in Figure 4), was selected for this case. The total permeable surface area is 0.74 km², comprising 31% parking areas and 69% roadside pavements and paths. As shown on the map, the sizes of permeable surface zones vary, but the optimisation process automatically normalises these differences through intervention costs.

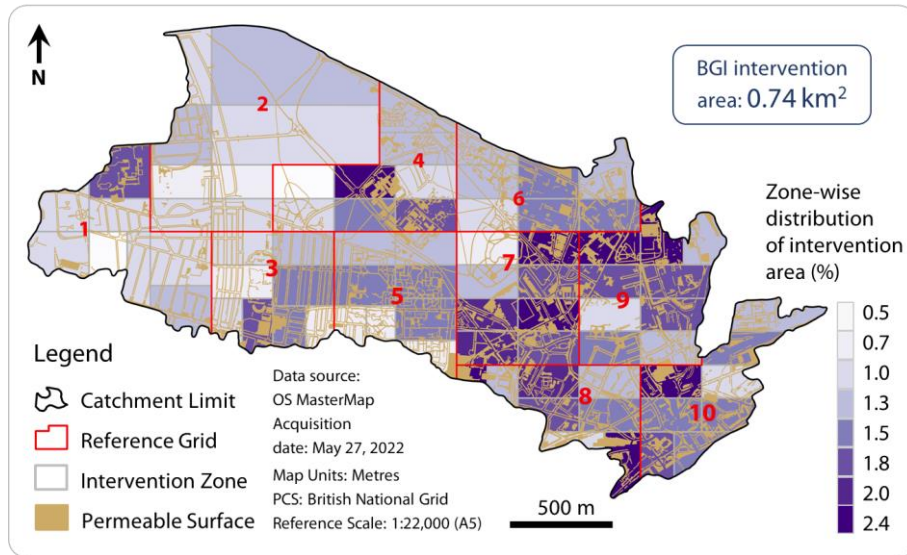


Figure 4. Permeable surface zonation for interventions.

2.6 Optimisation framework

The optimisation framework integrates a Multi-Objective Optimization Algorithm (MOOA) (Venter, 2010), called the Non-dominated Sorting Genetic Algorithm (NSGA-II) (Deb et al., 2002), with the CityCAT flood simulation model to identify the most cost-effective spatial combinations of permeable surface zones. MOOAs generally solve optimisation problems by iteratively changing the values of decision variables in a set of candidate solutions, called population, to achieve better values for considered objective functions. This iterative process, known as generations, continues until a termination criterion is reached. The result is a set of optimal solutions called the Pareto optimal front, representing the best trade-offs between objective functions (Maier et al., 2019). NSGA-II, in particular, uses non-dominated sorting to identify the optimal solutions and applies a crowding distance method to maintain population diversity to create better solutions in the new generation (Deb et al., 2002). The following sections provide an overview of the problem framing applied in this study.

2.6.1 Decision variables and objective functions

The decision variables include the centroid locations of the permeable surface zones. Each zone is assigned a unique index (I_j where $j = 1, 2, \dots, 80$). Candidate solutions are combinations of the 80 zones, with each zone represented by a gene and encoded in binary format: ‘1’ indicates that a zone is available, while ‘0’ means the zone is not available. The objective functions are the life cycle cost (LCC) of the permeable surface

zones and the associated levels of risk (R) to properties. Based on these decision variables and objective functions (LCC, R), the optimisation problem can be written as:

$$\text{Minimize: } F(I) = (F_{LCC}, F_R)$$

The LCC for the j^{th} permeable zone can be computed using the following equation:

$$LCC(I_j) = (C_c + C_o) \times S(I_j) \quad j = 1, \dots, 80$$

C_c and C_o are the unit size capital and operational costs, respectively, and $S(I_j)$ is the j^{th} permeable surface zone area. The capital cost refers to the one-time installation expense, while the operational cost is the annual maintenance expense of the permeable surfaces over a specific lifetime.

The LCC per unit of permeable surface area was calculated following the guidelines from the UK Environment Agency (Gordon-Walker et al., 2007). An average inflation rate of 2.9% was applied to calculate the current cost using the equation below.

$$FV = BV(1 + i)^n$$

Where: FV represents the future value, BV is the base year value, i is the inflation rate, and n is the number of maintenance years. For this study, the operational cost was multiplied by the lifespan of the permeable surface, which is 40 years, before being added to the capital cost.

2.6.2 Single return period-based BGI optimisation

Previously, Ur Rehman et al. (2024) used the number of buildings exposed to flooding as a risk objective function. The criteria for calculating the building's exposure is based on the 90th percentile and the mean of maximum flood depth around the building. When optimising BGI with the subject risk function, the exposure tool only records the effectiveness of the BGI feature if it reduces the 90th percentile and the mean of maximum flood depth around a building to a certain level, making the risk objective function discrete in its working. The discreteness of risk function can underestimate the efficiency of BGI interventions and can lead to contrasting patterns of BGI performance across different rainstorm intensities. On the other hand, a continuous risk objective function, such as direct damage cost (DDC) to the buildings, can record the contribution of BGI features for all ranges of flood depth reduction,

potentially providing more consistent risk mitigation. The DDC is calculated using the depth-damage curves method introduced in the Multi-Coloured Manual (MCM) for economic appraisal (Pening-RowSELL et al., 2014). The depth-damage curve approach calculates DDC for different types of buildings according to the flood depths around those buildings. Figure 5 presents the damage values for various building types based on different flood depths. The MCM considers the DDC per property for residential buildings (Figure 5a) and the DDC per unit area for non-residential buildings (Figure 5b). The DDC per unit area is then multiplied by the total building area to calculate the total DDC for non-residential buildings. DDC is calculated for a wide range of flood depths, so it is expected to work as a continuous risk objective function during BGI optimisation.

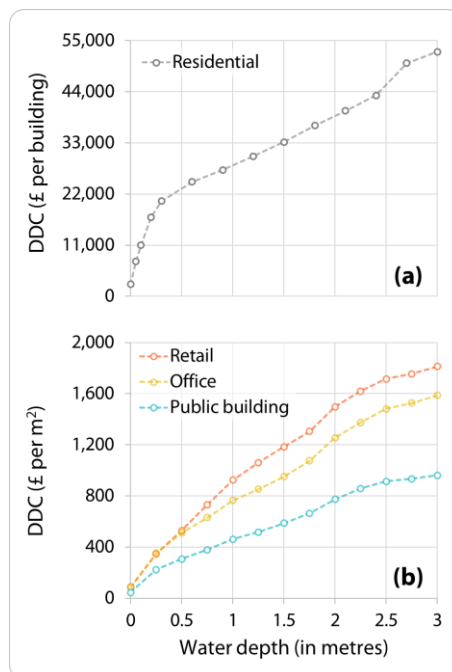


Figure 5. Depth damage curves for (a) non-residential and (b) residential buildings

The schematic diagram of the multi-objective optimisation framework is illustrated in Figure 6. It comprises NSGA-II, CityCAT, and Risk Modules. Initially, NSGA-II (Figure 6a) randomly generates 'P-2' candidate solutions, each representing different combinations of permeable surface zones. The first candidate solution, with no permeable zones, defines the baseline scenario, while the Pth candidate solution, with all permeable zones, represents the maximum intervention scenario. Next, NSGA-II passes these candidate solutions to the objective functions for fitness evaluation. The cost function calculates the LCC of each candidate solution using the formula provided below:

$$LCC(S_z) = \sum_{j=1}^{80} LCC(I_j) \quad \text{where } z = 1,2,3,\dots,P \\ I_j \neq 0$$

$LCC(S_z)$ is the life cycle cost for the z^{th} candidate solution, and $LCC(I_j)$ is the life cycle cost of the j^{th} permeable intervention zone.

Similarly, the risk function processes the 'P' candidate solutions sequentially using the CityCAT module (Figure 6b). This module consolidates geometry files of the available permeable surface zones in each solution. Then, it incorporates standard inputs such as rainfall, DEM, and geometries of green areas and building footprints to compute maximum water depths. These water depths are then forwarded to the risk module (Figure 6c), which is adapted from Bertsch et al. (2022). The risk module creates a buffer around each building at 150% of the DEM grid cell dimension. The buffer polygons are overlaid on the flood depth map to extract flood depth cells surrounding each building. The risk module then calculates the 90th percentile and mean of maximum depth values within each building buffer area to determine whether the building B_i (where $i = 1, 2, \dots, m$) is at risk or not at risk. If B_i is categorised as at risk, the DDC is calculated using the 90th percentile of the water depth value, which helps tackle outliers in maximum flood depth values. The building classification approach helps avoid extra DDC for buildings with negligible water depths. The total risk is the sum of DDCs for 'm' buildings, calculated using the following equations:

$$DDC(S_z) = \sum_{i=1}^m \begin{cases} I_{R_i} \times DDC_{res_d_{90th_i}} & B_i \text{ is residential} \\ I_{R_i} \times A_{B_i} \times DDC_{non-res_d_{90th_i}} & B_i \text{ is non-residential} \end{cases} \quad z = 1,2,3,\dots,P \quad (1)$$

$$I_{R_i} = f(d_{m_i}, d_{90th_i}) = \begin{cases} 0 & d_{m_i} < 0.1 \text{ m AND } d_{90th_i} < 0.3 \text{ m} & B_i \text{ not at risk} \\ 1 & \text{Otherwise} & B_i \text{ at risk} \end{cases} \quad (2)$$

Where:

- $DDC(S_z)$ is the direct damage cost (risk level) for the z^{th} candidate solution.
- I_{R_i} is the risk index, a function of the mean maximum depth (d_{m_i}) and the 90th percentile of maximum depths (d_{90th_i}) around the i^{th} building B_i . The criterion for I_{R_i} is adapted from the exposure classification scheme presented by Bertsch et al. (2022).

- $DDC_{res_d90th_i}$ is the direct damage cost for a residential building based on the 90th percentile of maximum flood depths around B_i .
- A_{B_i} is the area of B_i , and $DDC_{non-res_d90th_i}$ is the direct damage cost per unit area for a non-residential building, depending upon the 90th percentile of maximum flood depths around B_i .

After receiving the LCCs and DDCs for ‘P’ candidate solutions, the NSGA-II module evaluates their fitness based on their ability to minimise both LCC and DDC simultaneously. The algorithm then checks the generation number as a termination criterion and stops if it is met. Otherwise, evolutionary operations, including parent selection, crossover, and mutation (Ur Rehman et al., 2024), create a new set of ‘P’ offspring. These offspring are evaluated for cost and risk objectives to determine their LCCs and DDCs. NSGA-II combines the LCCs and DDCs of both parent and offspring populations, selects the ‘P’ best solutions, and forms a new generation of parents. This process repeats for N generations to achieve optimal solutions with the lowest LCC and DDC.

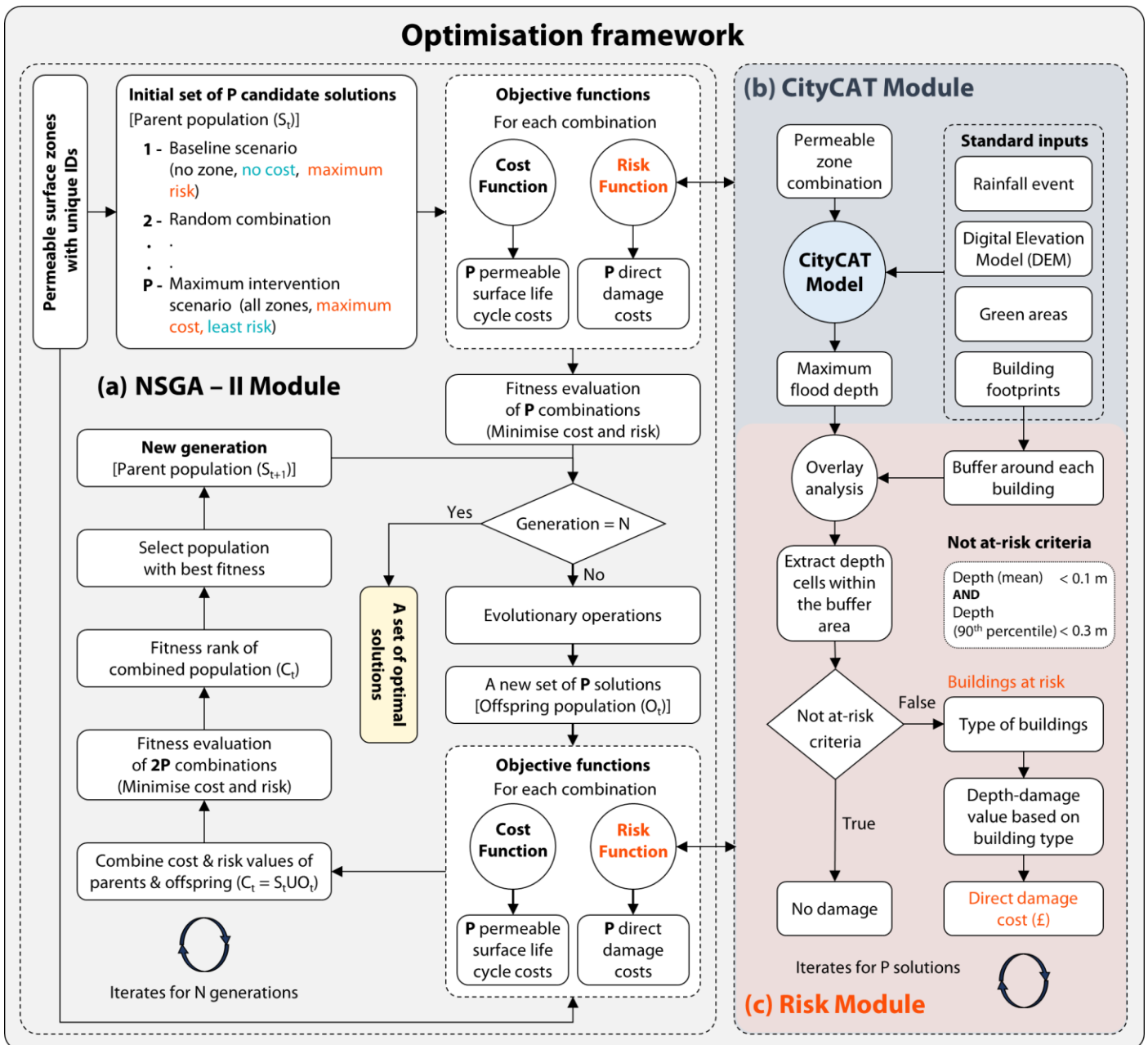


Figure 6. The optimisation framework for individual return periods integrates (a) NAGA-II, (b) CityCAT, and (c) Risk modules.

2.6.3 Multiple return period-based BGI optimisation

For multiple return periods, each return period has an associated direct damage cost (DDC), resulting in multiple DDCs. However, a multi-objective algorithm cannot handle more than three DDCs. A potential solution could be a many-objective optimisation algorithm (Deb & Jain, 2014), which can process multiple DDCs simultaneously. However, implementing such an algorithm is complex, and the equal weighting of DDCs for shorter and longer return periods makes it unsuitable for this problem. Instead, a weighted aggregation of DDCs into a single risk objective function, such as expected annual damage (EAD), is more appropriate. EAD, calculated using the trapezoidal rule, assigns weights to DDCs based

on exceedance probability (Bilskie et al., 2022). Five return periods ($T = 10, 20, 30, 50,$ and 100 years) were selected to balance accuracy and computational cost, as Ward et al. (2011) noted that using very few return periods may overestimate EAD. Adopting EAD as a risk objective also enables calculating realistic lifetime cost benefits for BGI. The following equation from the Scottish Government (2018) was used to compute EAD:

$$EAD(S_z) = \frac{1}{2} \left[\begin{array}{l} (DDC(S_z)_{T10} + DDC(S_z)_{T20}) \times \left(\frac{1}{10} - \frac{1}{20}\right) + \\ (DDC(S_z)_{T20} + DDC(S_z)_{T30}) \times \left(\frac{1}{20} - \frac{1}{30}\right) + \\ (DDC(S_z)_{T30} + DDC(S_z)_{T50}) \times \left(\frac{1}{30} - \frac{1}{50}\right) + \\ (DDC(S_z)_{T50} + DDC(S_z)_{T100}) \times \left(\frac{1}{50} - \frac{1}{100}\right) + \\ (DDC(S_z)_{T100} + D(S_z)_{INFIN}) \times \left(\frac{1}{100} - 0\right) \end{array} \right] \text{ where } z = 1, 2, \dots, P \quad (3)$$

$$D(S_z)_{INFIN} = DDC(S_z)_{T100} + (DDC(S_z)_{T100} - DDC(S_z)_{T50}) \times \left(\left(\frac{1}{100} - 0\right) / \left(\frac{1}{50} - \frac{1}{100}\right) \right) \quad (4)$$

The term $D(S_z)_{INFIN}$ is used to get proportionate direct damage contributions from the 100-year return period in the absence of the next longer return period.

The adaptation of a multi-objective optimisation framework for composite return periods is shown in Figure 7. While the processes in the NSGA-II module remain unchanged, the CityCAT and risk modules evaluate each candidate solution across all return periods, calculating individual DDCs and then the EAD for each solution. This process is repeated ‘P’ times to generate ‘P’ EADs. The NSGA-II module then optimises over N generations using the LCC and EAD values of the candidate solutions.

Supplementary information S3 provides the NSGA-II parameters and values used for single- and multiple-return-period optimisation.

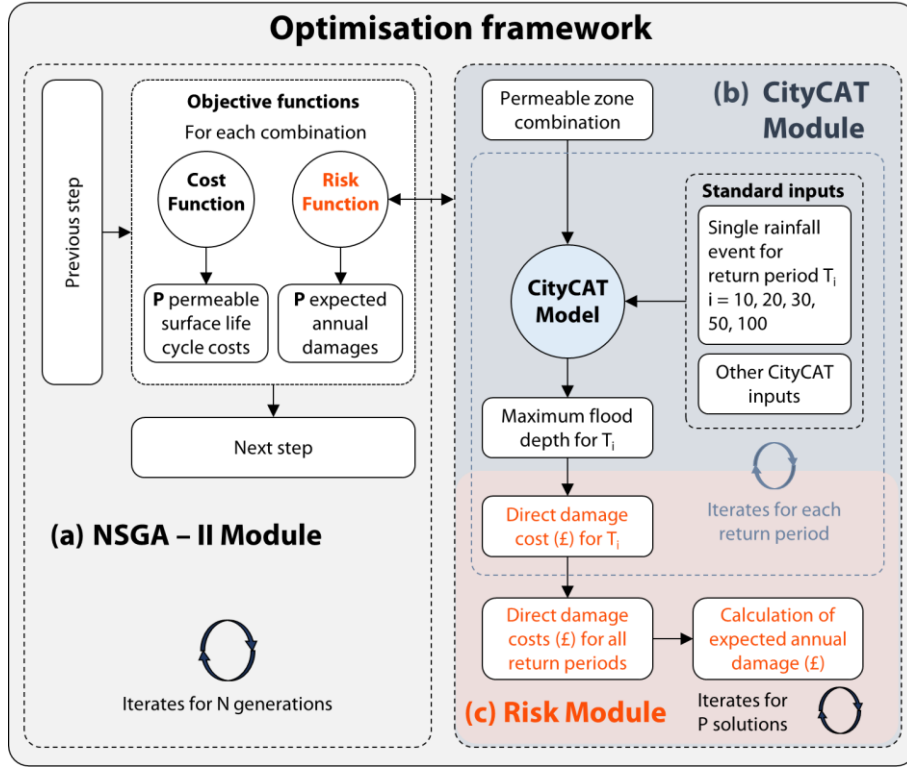


Figure 7. The optimisation framework for the composite of multiple return periods. This figure should be interpreted in conjunction with Figure 6

2.7 Optimisation performance quantification

Three metrics, Maximum Risk Difference (MaxRD), Median Risk Difference (MedRD), and Area Under Pareto Front (AUPF), were developed to quantify the performance and robustness of Pareto fronts obtained for the 100-year and composite return period optimisation (trialled Pareto fronts). Pareto fronts obtained by optimising BGI for individual return periods were used as a reference.

Maximum Risk Difference (MaxRD) and Median Risk Difference (MedRD) quantify the largest and median disparity in risk (DDC) between the reference and trialled Pareto fronts at any BGI cost (LCC). MedRD represents the central tendency of the risk discrepancies, providing a robust measure less sensitive to extreme deviations than the maximum difference. The formulas for these metrics are provided below:

$$MaxRD = \max_{c \in C} |R_{trial}(c) - R_{ref}(c)| \quad (5)$$

$$MedRD = median(|R_{trial}(c_1) - R_{ref}(c_1)|, |R_{trial}(c_2) - R_{ref}(c_2)|, \dots, |R_{trial}(c_n) - R_{ref}(c_n)|) \quad (6)$$

Where:

$R_{ref}(c)$ and $R_{trial}(c)$ represent the risk value (DDC) on the reference and trialled Pareto fronts for a given cost c . $C = \{c_1, c_2, \dots, c_n\}$ denotes the set of all cost values (LCC) where the solutions of Pareto fronts are evaluated.

MaxRD and MedRD metrics can also be expressed as percentages of the total risk range. The total risk range (R_{range}) is defined as the difference between the risk of the baseline or no intervention solution ($DDC_{Baseline}$) and the maximum intervention solution with the highest LCC ($DDC_{Max-int}$).

$$MaxRD (\%) = \frac{MaxRD}{R_{range}} \times 100 \quad (7)$$

$$MedRD (\%) = \frac{MedRD}{R_{range}} \times 100 \quad (8)$$

$$R_{range} = DDC_{Baseline} - DDC_{Max-int} \quad (9)$$

Area Under Pareto Front (AUPF) measures the total area beneath a Pareto front in the objective space, defined by the BGI cost (LCC) and risk (DDC). This metric captures the performance of the entire Pareto front distribution. A smaller area typically indicates a more optimal front, representing lower cost and risk. AUPF is computed using the trapezoidal rule, as defined in the equation below:

$$AUPF = \sum_{i=1}^{n-1} \frac{(c_{i+1} - c_i) \times (R(c_i) + R(c_{i+1}))}{2} \quad (10)$$

Where:

$C = \{c_1, c_2, \dots, c_n\}$ represents the set of sorted cost values (LCC) and $R(c_i) =$ risk value (DDC) at cost c_i .

The difference in underneath areas ($\Delta AUPF$) between the reference ($AUPF_{ref}$) and trialled Pareto fronts ($AUPF_{trial}$) reflects the overall disparity in the trialled set of solutions. This disparity can be expressed as a percentage of the reference AUPF.

$$\Delta AUPF (\%) = \frac{\Delta AUPF}{AUPF_{ref}} \times 100 \quad (11)$$

$$\Delta AUPF = AUPF_{trial} - AUPF_{ref} \quad (12)$$

2.8 Benefit-cost analysis of optimised BGI solutions

Integrating BGI LCC and EAD in multiple-return periods-based optimisation provides an opportunity to calculate more realistic benefit-cost ratios by accounting for the lifespan of the BGI. The following equation was used to compute benefit-cost ratios for optimised solutions:

$$B/C = \frac{(EAD_{Baseline} - EAD_{BGI}) \times BGI \text{ lifespan}}{BGI \text{ LCC}} \quad (13)$$

Where:

- B/C represents the benefit-cost ratio.
- BGI lifespan is the time (in years) when substantial maintenance or overhauling of the BGI is required.
- BGI LCC is the life cycle cost of the BGI, calculated based on its lifespan.
- $EAD_{Baseline}$ is the expected annual damage for the baseline flooding scenario (i.e., without BGI intervention).
- EAD_{BGI} is the expected annual damage after implementing a specific BGI solution.

3 Results and discussion

3.1 Optimisation for individual return periods

The BGI optimisation results for individual return periods are shown in Figure 8a-e. Referring to the scatter plots, the x- and y-axes represent the BGI life cycle cost (LCC) and the buildings' direct damage cost (DDC), respectively. Grey dots in the plots depict solutions generated throughout the evolutionary process of NSGA-II, whereas the coloured dots indicate the optimal or best solutions achieved by the final generation. The optimal solutions for each return period form a curve, representing the Pareto optimal front. On each Pareto front, the solution positioned at the top-left represents the baseline scenario, while the bottom-right solution corresponds to the maximum intervention scenario. The latter indicates that the solution has the most permeable surface zones with the highest LCC. Additionally, for each return period, an individual spatial map highlights the contribution of each permeable surface zone to the optimal solutions. Zones with the highest contribution, indicated in dark blue, are considered highly cost-effective, while zones in orange shades are the least cost-effective. Zones with no contribution to risk reduction are shown in white.

Figure 8a-e highlights BGI's performance in reducing DDC and identifying the best zones for permeable interventions. The Pareto curve for the 50-year return period achieves greater depth than any other return period, indicating that optimal solutions with smaller LCCs (up to ~£10 million) result in a higher reduction in total DDC than other return periods with similar LCCs. In contrast, the Pareto curve for the

30-year return period has relatively low curvature towards minimal value. This variation is likely due to the catchment's hydrodynamics across different return periods and how the risk function operates. Different rainfall intensities result in varying water depths around buildings, and the effectiveness of permeable intervention zones depends on the generated surface runoff and flow pathways. For the 50-year return period, a smaller fraction of the total available permeable area effectively reduces water depths around buildings, leading to a substantial decrease in DDC. Another factor could be the type of buildings exposed during each return period. As shown in Figure 1, non-residential buildings typically have larger footprint areas and are more likely to be exposed to a higher DDC. It is evident from Figure 9 that more non-residential buildings are at risk during the 50- and 100-year return periods. Initially, only a few permeable surface zones seem to reduce DDC more effectively for the 50-year return period, as suggested by Figure 9a-b.

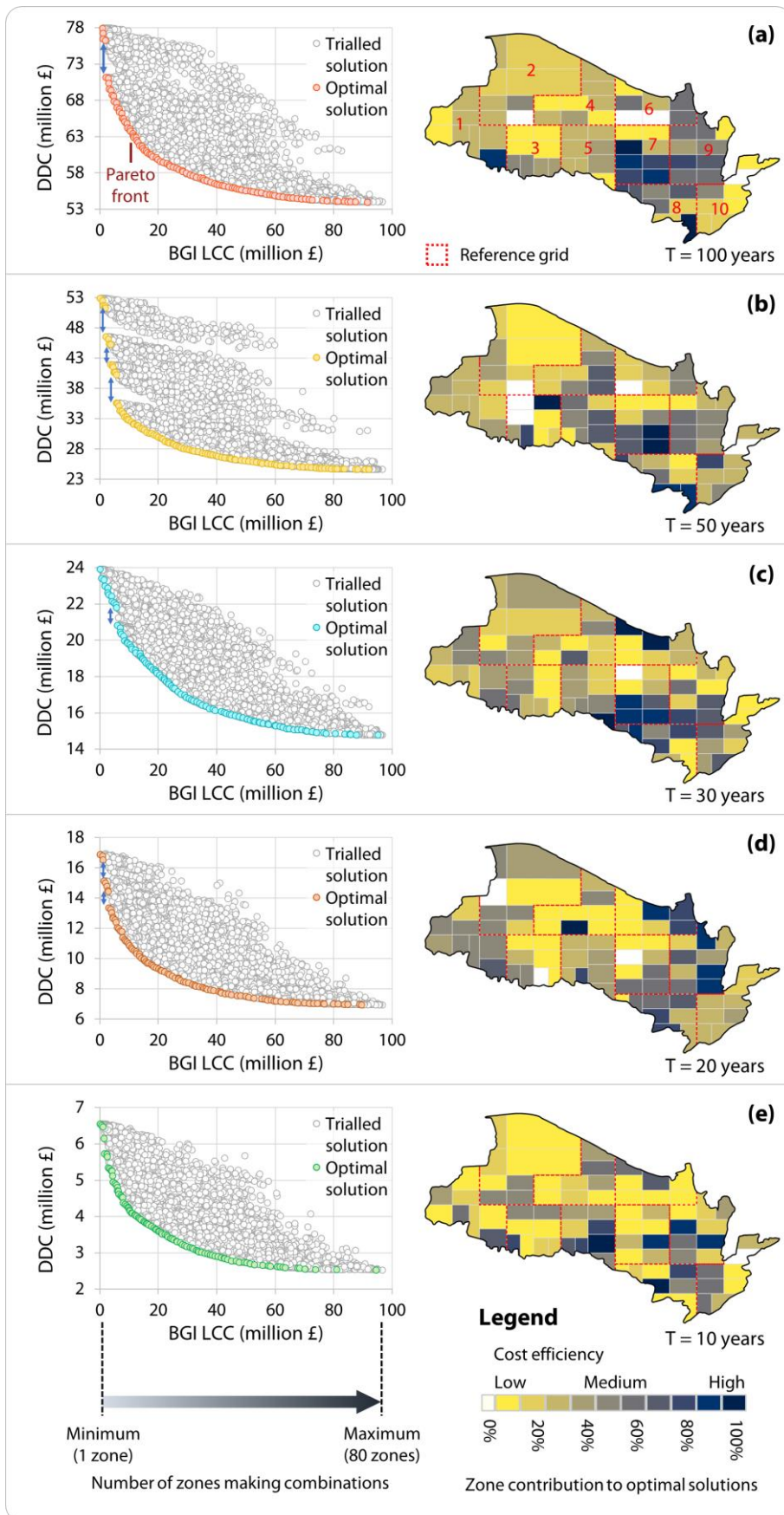


Figure 8. Optimisation of permeable zones for (1) 100-year, (b) 50-year, (c) 30-year, (d) 20-year, and (e) 10-year rainstorm return periods.

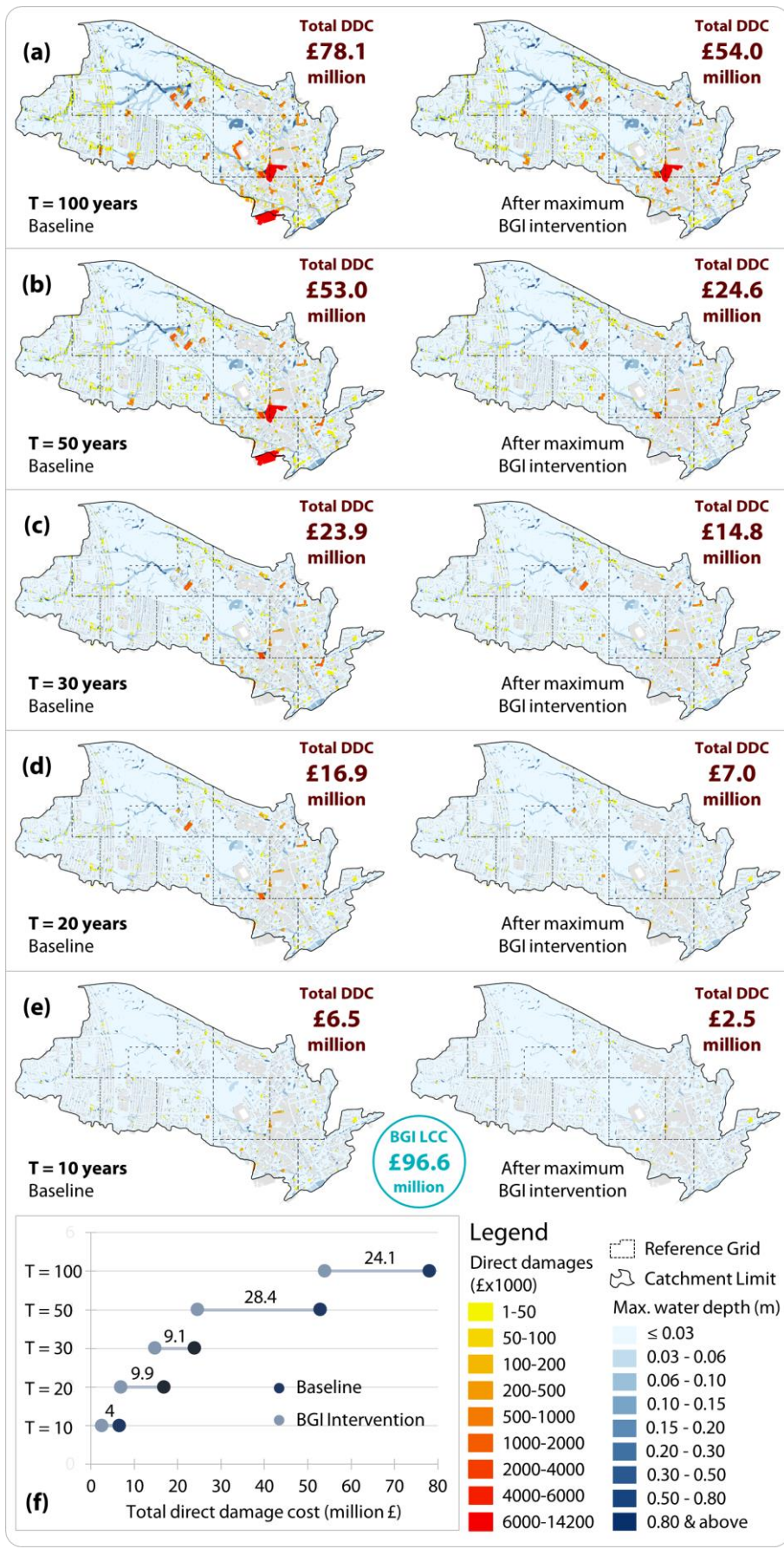


Figure 9. Direct damage cost to buildings calculated for baseline (left) and after implementing maximum BGI intervention (right) for (a) 100-year, (b) 50-year, (c) 30-year, (d) 20-year and (e) 10-year return periods, (f) shows the DDC ranges reduced by maximum intervention for considered return periods.

Another notable observation in the distinct Pareto fronts is the gaps between successive optimal solutions (see the blue line arrows along the y-axes in Figure 8a-d). These gaps can be attributed to the formulation of the risk function, as explained below:

- i. BGI interventions reduce the water depth around a building. If the water depth does not meet the ‘not at risk’ criteria outlined in equation (2), the building remains at risk but with a reduced DDC.
- ii. If the BGI intervention reduces the water depth to a level that meets the ‘not at risk’ criteria, the DDC for that specific building becomes zero.

The first type of DDC reduction, while the building is still at risk, is more gradual. However, the second situation can cause an abrupt decrease in total DDC. This observation is particularly true for non-residential buildings, where a minimal intervention (small LCC) that slightly reduces water depth to meet ‘not at risk criteria’ can prevent a large building from being at risk, leading to a higher DDC reduction and the gaps between successive solutions on the Pareto fronts. For further clarification, please refer to supplementary information S4.

In terms of the cost efficiency of permeable zones by location, the zone contribution maps in Figure 8a-e show varied results. For the 100-year return period, the cost-effective zones are relatively clustered (see reference grid cells 7, 8, and 9 in Figure 8a). However, the cost-effective zones start dispersing across the catchment when moving towards lower return periods (Figure 8b-e). The cost-effective zones for the 100- and 50-year return periods share some commonalities, but the maps for shorter and longer return periods show minimal similarities.

The clustering and dispersal of cost-efficient permeable zones from longer to shorter return periods can again be attributed to catchment hydrodynamics and building types. During high-intensity rainstorm events, such as the 100-year return period, water flows across the different regions of the catchment from the northwest to the southeast (Figure 9a). These regional flow paths combine with local surface runoffs, putting many non-residential buildings in reference grid cells 7, 8, and 9 at risk. Consequently, permeable zones in these grids not only infiltrate local surface runoff but also intercept flow paths from the upper parts of the catchment, reducing water depth around non-residential buildings and making a cluster of cost-effective zones in this region. For lower-intensity rainstorms, such as the 10-year return period

(Figure 9e) with probably no flow paths from the upper catchment, risk to the buildings is predominantly influenced by local surface runoff, resulting in scattered cost-effective zones. Other return periods between the 100- and 10-year follow a similar mechanism with varying contributions from local and regional runoffs.

3.2 Assessment of 100-year optimised Pareto front across other return periods

Figure 10a-d shows the results of the 100-year-optimised Pareto front evaluated for other return periods. The blue dots in the scatter plots represent optimised solutions for specific return periods, while the red dots indicate solutions optimised for the 100-year return period but assessed for others. The performance metric AUPF for the reference Pareto front is shown in light blue, while AUPF for the 100-year Pareto front is depicted in light blue plus reddish-filled areas. Similarly, MedRD and MaxRD are represented by blue and red dotted lines, respectively. It is clear from the scatter plots that the Pareto front optimised for the 100-year return period deteriorates when evaluated for other return periods. Aligning with earlier discussion on clustering and dispersal of cost-effective zones (Figure 8), performance metrics confirm that the 100-year Pareto front deterioration is moderate for closer return periods (30- and 50-year periods) but substantially higher for distant periods (20- and 10-year periods). AUPFs for the 20- and 10-year periods are 132% and 153% higher than the reference AUPFs. Similarly, MedRD and MaxRD, expressed as percentages of the total risk range, are higher for the 20-year (32% and 47%) and 10-year (36% and 58%) return periods. For the 30- and 50-year periods, while MaxRD (32% and 40%) remains higher, MedRD (15% and 10%) and AUPF (53% and 73% above reference) exhibit moderate differences.

Examining Figure 8 and Figure 10, the initial solutions on Pareto fronts include either a single best zone or combinations of a few top-performing zones. As LLC increases, additional zones, ranging from good to less effective, are incorporated. Since the most cost-effective zones and combinations in the 100-year optimisation differ from others, they perform poorly, especially for shorter return periods (10-, 20-year). However, discrepancies are relatively smaller at the Pareto fronts' tail, where reference and 100-year fronts already include some less-effective zones. These results indicate that the effectiveness of permeable surface zone locations and combinations is highly sensitive to rainfall intensity, demonstrating that

optimisation based on single maximum return periods fails to deliver robust solutions for rainfall variations.

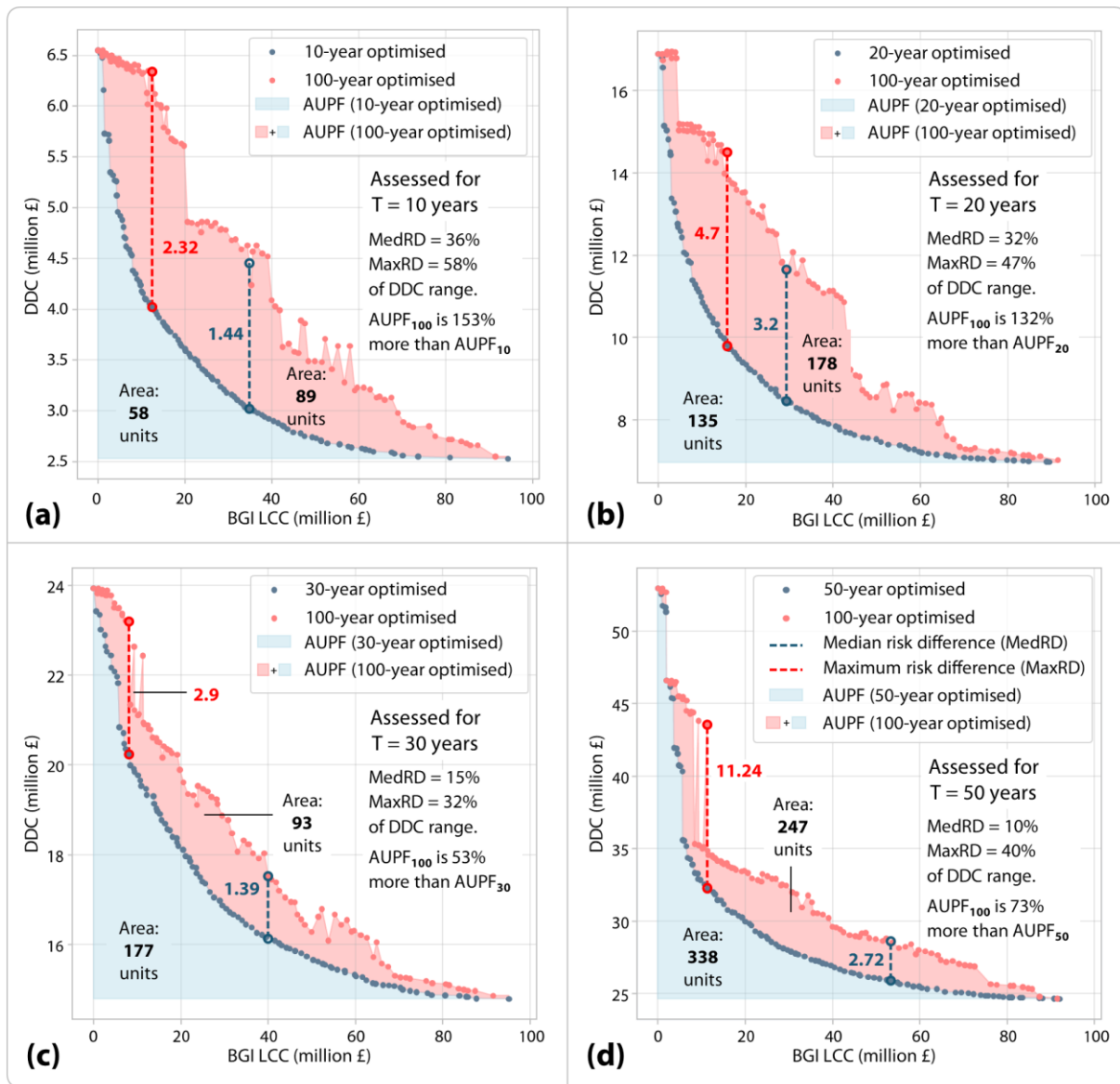


Figure 10. Solutions optimised for a 100-year rainstorm return period are assessed for (a) 50-year, (b) 30-year, (c) 20-year, and (d) 10-year rainstorm return periods.

The findings of this study are generally aligned with very limited results (100- and 30-year evaluations only) reported by Ur Rehman et al. (2024). However, the comparison of the 100-year return period Pareto front assessed for the 30-year return period shows a relatively low discrepancy, possibly due to the formulation of the continuous risk objective function in this study. When comparing cost efficiency by zone, spatial patterns differ between the studies due to variations in the risk objective function. The reference study, using a discrete risk function based on the count of buildings exposed to flooding, gives equal weight to all buildings, favouring cost-effective zones in residential areas. In contrast, the current study uses a continuous risk function based on DDC, shifting cost-effective zones to non-residential areas

due to larger building footprints and associated damage costs. Additionally, the continuous risk function in this study effectively captures even minor flood reductions, resulting in fewer ‘no contribution’ zones compared to a larger number of ‘no contribution’ zones in the reference study. The comparative results emphasise the importance of carefully selecting a risk objective function as it can significantly influence the cost-effective locations for BGI interventions.

3.3 Optimisation for a composite of multiple return periods

The BGI optimisation results based on multiple return periods are shown in Figure 11a-c. In Figure 11a, the scatter plot displays BGI life cycle cost (LCC) along the x-axis and expected annual damage (EAD) along the y-axis, with grey dots representing generated solutions and blue dots representing optimal Pareto front solutions. Figure 11c shows the Pareto front’s position on the DDC scale for the selected five return periods. EAD for each optimal solution is calculated using DDC values across all return periods, as per equations (3) and (4). Although the 100- and 50-year return periods are weighted less due to lower exceedance probabilities (3), their higher DDC values make them the largest contributors to EAD. Conversely, the 10-year return period contributes the least, as it appears only once in the EAD calculation. Figure 11b presents a spatial map of the catchment area, highlighting the contribution of individual permeable surface zones to the Pareto front solutions. An animation of the multi-return period optimisation is available in Appendix B.

Figure 11c shows that the EAD-derived Pareto front remains near-optimal on the DDC scale for most return periods, except for the 50-year one, where a section of the Pareto front is suboptimal within the 28–35 million DDC range. This discrepancy likely arises from variations in catchment hydrodynamics and the DDC-based risk function (section 3.1 for details). Unlike Pareto fronts based on individual return periods, solutions on the EAD scale (Figure 11a) remain evenly distributed due to variations in BGI performance across different rainfall intensities, balancing overall cost-effectiveness and preventing dips along the risk axis.

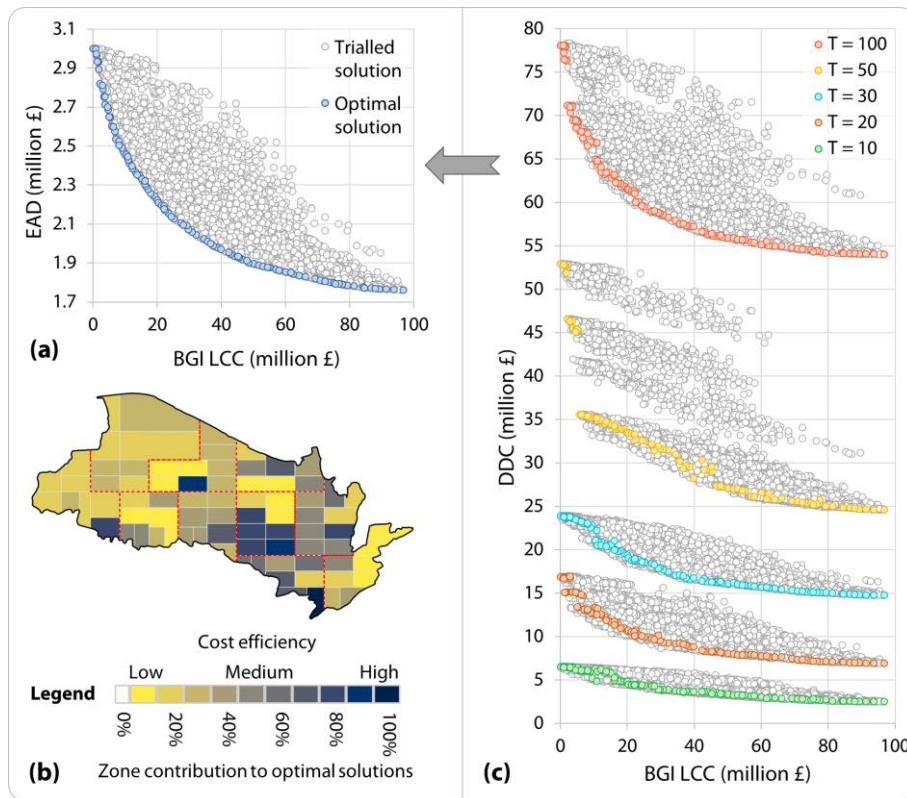


Figure 11. Multiple-return period-based BGI optimal and trialed solutions on (a) EAD and (c) DCC scales, (b) represents the contribution of permeable surface to composite optimised Pareto front.

A comparison of zone contribution maps for composite optimisation (Figure 11c) and individual return period-based optimisation (Figure 8a-e) shows the composite map aligns more closely with the 100- and 50-year maps, with some similarity to the 30- and 20-year maps, and minimal overlap with the 10-year map. This pattern is expected, as BGI in higher return periods typically achieves greater DDC reductions (Figure 9 and Figure 11c), strongly influencing zone cost-effectiveness calculations.

To assess the impact of the number of return periods used to calculate EAD, supplementary information S5 compares EAD values calculated using five return periods ($T = 10, 20, 30, 50, 100$) versus three ($T = 10, 30, 100$), showing that fewer return periods overestimate EAD values, consistent with Ward et al. (2011).

3.4 Optimisation performance evaluation

The performance of the composite-optimised Pareto front in relation to reference and the 100-year Pareto fronts is depicted in Figure 12a-d. The figure implies that, although the composite-optimised Pareto front does not precisely align with the reference fronts for individual return periods, it demonstrates improvements across all performance metrics and return periods compared to the 100-year-optimised

Pareto front. Quantification of relative improvements in performance metrics (Figure 13) reveals the highest improvements in AUPF (73%) and MedRD (22%), and the second-highest in MaxRD (13%) for the 20-year return period. For the 10-year return period, MaxRD, MedRD, and AUPF improved by 2%, 16%, and 39%, respectively. In the 50-year return period, MaxRD improved by 23%, MedRD by just 4%, and AUPF by 26%. Conversely, the 30-year return period achieved a slightly better improvement in MedRD (7%) and a relatively smaller improvement in AUPF (15%), with no improvement in MaxRD. Supplementary information S6 and S7 provide detailed statistics for these comparisons.

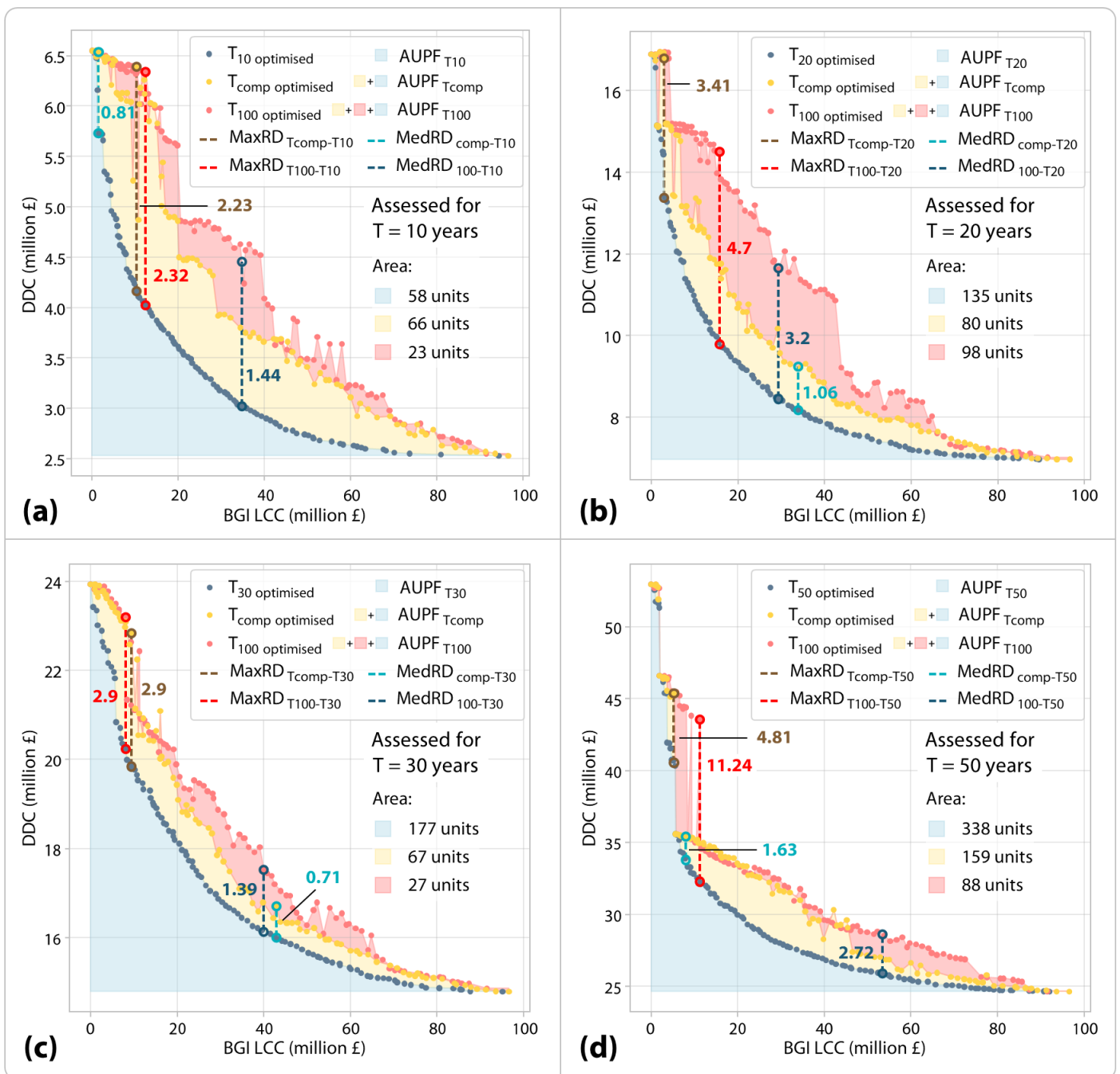


Figure 12. Solutions optimised for a 100-year and composite rainstorm return period are assessed for (a) 50-year, (b) 30-year, (c) 20-year, and (d) 10-year rainstorm return periods.

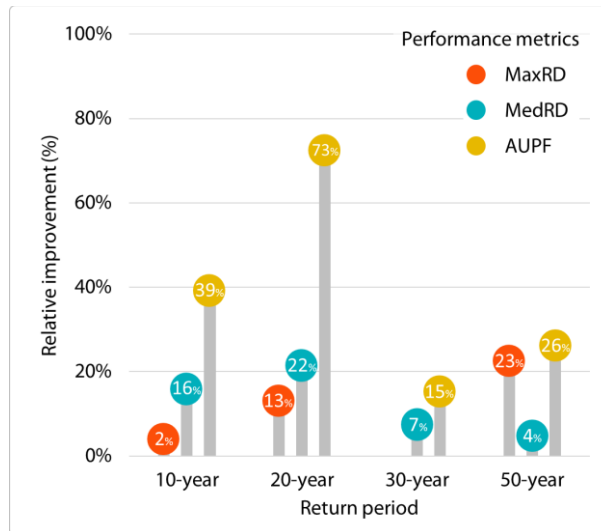


Figure 13. Improvement in performance metrics for the composite-optimised Pareto front compared to the 100-year-optimised front.

Reflecting on the composite-optimised solutions, achieving their simultaneous alignment with all four Pareto fronts optimised for individual return periods is nearly impossible. The goal is to find the best trade-offs that minimise disparities across all return periods, thereby introducing robustness into the BGI design. Composite optimisation achieves this by proportionally considering risk reductions from each return period during EAD calculation. As shown in Figure 8c, a few solutions are slightly suboptimal for the 100-year return period on the DDC scale. However, this trade-off is beneficial, as minimal degradation in the 100-year performance leads to significant improvements in BGI efficiency for other return periods. Figure 12 illustrates that longer return periods generally exhibit larger DDC ranges and greater maximum and median DDC differences than shorter ones. Nevertheless, low- to moderate-intensity rainstorms, which occur more frequently, make it critical to consider BGI performance across shorter return periods. Adopting EAD as a risk objective function effectively addresses this balance, though longer return periods still exert a strong influence as BGI reduces higher DDC in those. Additionally, the use of $D(S_Z)_{\text{INFIN}}$ in equation (4) maintains a significant focus on the 100-year return period while facilitating improvements in other return periods. For instance, despite contributing only once during EAD calculation in equation (3), solutions still see improvement on the 10-year return period scale. Overall, a BGI design based on composite optimisation is more robust than one based on a 100-year (single maximum) return period. The variation in the performance of the proposed design across return periods is influenced by catchment

hydrodynamics and the non-linear effectiveness of BGI in reducing damage across different rainfall intensities (see Section 3.1 for discussion).

3.5 Benefit-cost analysis

Figure 14 illustrates the benefit-cost ratios of solutions in the composite Pareto front (Figure 11a) calculated using the equation (13). The figure on the x-axis represents the BGI life cycle cost (LCC) in million £, while the y-axis shows the benefit-cost ratio. As shown in (8), an increase along the x-axis indicates an increase in permeable surface zones or the overall permeable area.

The benefit-cost ratio demonstrates a sharp rise starting from the plot's baseline solution at the origin (0, 0). After reaching its maximum of 3.6 when BGI LCC is £2 million, the benefit-cost ratio gradually declines, eventually reaching a minimum of 0.5 at the maximum BGI LCC value of £96.6 million. This observation suggests that initial investments in BGI provide substantial benefits relative to costs.

These results indicate that a couple of initial solutions (after baseline), which involve minimal zone combinations (e.g., only one or two zones), have relatively low benefit-cost ratios due to their limited impact on damage reduction. However, as additional zones are introduced, the optimisation algorithm identifies good combinations that significantly reduce damage costs. This substantial reduction is likely due to some large, high-risk, non-residential buildings transitioning from “at-risk” to “not-at-risk,” thereby boosting the benefit-cost ratio. As the BGI LCC increases beyond the point of maximum benefit-cost, the values of the benefit-cost gradually decline, indicating that additional permeable zones do not proportionally reduce the damages to the buildings. This shrinking return suggests that beyond a certain investment level, further BGI interventions yield progressively smaller reductions in damage. Overall, the benefit-cost ratios for BGI interventions remain low, with the most effective return on investment up to BGI LCC values of £5 million.

The lifetime benefit-cost ratios of permeable surface interventions remained low. Catchment-specific factors contributing to this low return include a relatively steep catchment gradient and low soil permeability in the study area. In steeper catchments, water flows rapidly, leaving less time for infiltration through permeable surfaces. Similarly, low soil permeability limits the volume of water that can infiltrate. Additionally, these BGI benefits are calculated solely based on reductions in direct damage costs to

buildings. Considering indirect costs, such as business interruption or loss due to building flooding, would likely increase the overall direct benefits.

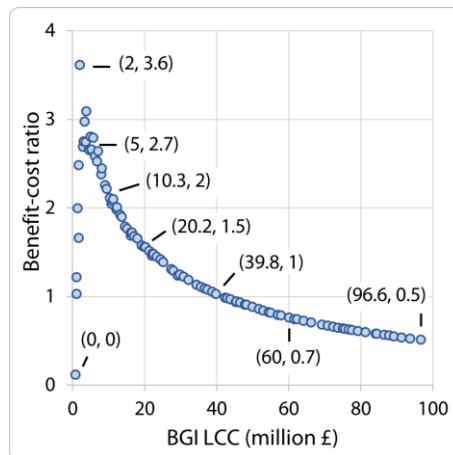


Figure 14. Scatter plots showing benefit-cost ratios for Pareto front

3.6 Climate change resilience assessment for composite BGI design

Climate change resilience for the composite BGI design was assessed by evaluating optimal solutions under three climate uplift scenarios applied to five baseline return periods. The results, including the Pareto front with uplifts applied and the corresponding benefit-cost ratios, are presented in Figure 15b and Figure 15c. Figure 15a repeats the zone cost-efficiency map, which is the same for both composite Pareto front and uplifts. Key observations and explanations are as follows:

- Shift in EAD values:** EAD values shift upwards with climate uplift, as higher rainfall intensities produce greater water depths around buildings, leading to increased DDC and EAD. Despite this intensification, BGI effectively reduces a broader range of EAD in climate uplift scenarios.
- Pareto front curvature:** The curvature of the Pareto front slightly reduces when moving from low to high climate uplift scenarios. Similar to the baseline (Figure 13a), there is a sharp reduction in EAD at the initial BGI LCC (up to ~£2 million). After this point, the rate of EAD reduction slows with increasing BGI LCC for all uplifts.
- Benefit-cost ratio patterns:** In the benefit-cost ratio graphs (Figure 15c), initial BGI investments follow a pattern similar to the baseline Pareto front, yielding higher benefit-cost ratios than subsequent investments. Interestingly, the climate uplift scenarios demonstrate better benefit-cost ratios than the baseline. This finding can be attributed to greater direct damages and EAD in

climate uplift scenarios, which enable BGI to achieve higher damage reductions (see the dotted coloured line indicating the EAD range in Figure 15b).

- Robustness of composite Pareto front:** Although a few gaps in the climate uplift fronts indicate an uneven distribution of some solutions, they remain intact overall, following the curvature line. This stability demonstrates the resilience of the proposed composite BGI design to climate-induced rainfall severity.

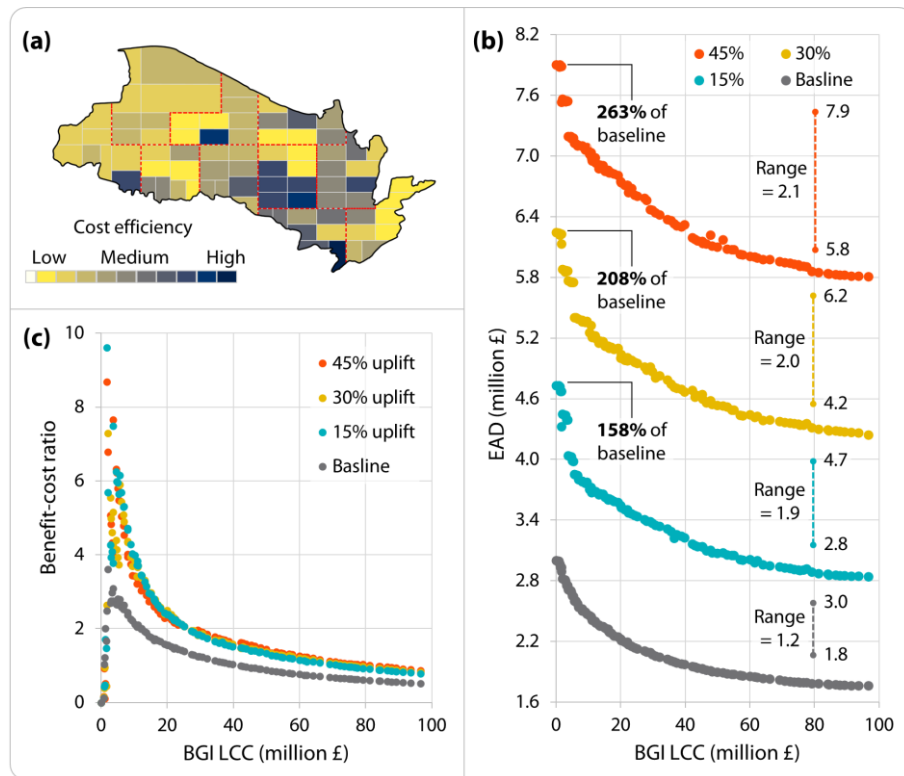


Figure 15. Composite optimisation-based (a) zone efficiency map, (b) Pareto front assessment for climate change uplifts, and (c) benefit-cost ratios for the uplifts.

4 Study limitations

- This study applies only the 2D surface flooding module of CityCAT and a 5-m spatial resolution DEM to avoid excessive computational costs associated with coupling the sub-surface drainage module and using a high-resolution DEM. These configurations were already applied in the reference study (Ur Rehman et al., 2024), so the same modelling environment was maintained for comparative analysis.
- BGI performance leans more towards reducing risk for non-residential buildings due to the area-based direct damage cost calculation. However, this method aligns with the UK standard for estimating direct damage costs for such buildings.

- In composite optimisation, BGI efficiency inclines more towards higher return periods due to greater direct damage cost reductions. Although the use of exceedance probabilities in calculating expected annual damage ensures proportional DDC contributions, additional weighting for lower return periods could enhance their influence in trade-off development.

5 Future recommendations

- To overcome high computational cost, users can use a limited, evenly sampled set of return periods for EAD calculation during optimisation, then simulate the resulting Pareto front across more return periods to refine EAD and benefit-cost ratios. Inconsistent solutions can be discarded in this process.
- This study considers only direct damage costs for optimisation. Users may include indirect costs, such as business and revenue loss, transport disruption, and impacts on emergency services, to develop a more comprehensive risk objective function. Additional BGI features, such as detention ponds and swales, are also recommended for improved returns.
- Calculating non-monetary benefits, such as groundwater recharge and water quality improvement, is recommended to evaluate the full value of permeable surface interventions.
- This study uses 30-minute rainstorm events for method demonstration. For effective BGI design, longer-duration events (60 minutes or more, depending on catchment size) are recommended.

6 Conclusions

This study explores multi-objective optimisation approaches to develop a robust blue-green urban flood risk management method. It integrates a Non-dominated Sorting Genetic Algorithm II (NSGA-II) with a fully distributed hydrodynamic model to identify the best locations and optimal combined size of Blue-Green Infrastructure (BGI) across five return periods ($T = 10, 20, 30, 50, \text{ and } 100$ years). Introducing direct damage cost (DDC) to different building types as a continuous risk objective function effectively captures the variability in BGI performance but shifts the location of the most cost-effective zones compared to results obtained in an earlier study using a discrete risk function. This finding highlights the importance of carefully selecting the risk objective function in optimisation-based BGI design. While DDC improves location-wise BGI performance within individual return periods, it did not yield a single

optimal BGI design applicable across all considered return periods. Performance metrics such as Maximum Risk Difference (MaxRD), Median Risk Difference (MedRD), and Area Under Pareto Front (AUPF) revealed a lack of robustness when a 100-year optimised design was tested for other return periods. Disparities were extreme for shorter return periods, with AUPF 153% and 132% higher than the reference Pareto front, MaxRD 58% and 47%, and MedRD 36% and 32% of the risk ranges for 10- and 20-year return periods, respectively. Nonetheless, DDC enabled the calculation of expected annual damage (EAD) as a composite risk objective function, integrating all five return periods within a multi-objective optimisation framework. The resulting composite BGI design showed improved applicability across all return periods, with enhanced AUPF (39%, 73%, 15%, 26%), MaxRD (2%, 13%, 0%, 23%), and MedRD (16%, 22%, 7%, 4%) for $T = 10, 20, 30,$ and 50 years, respectively. These results demonstrate that EAD effectively accounts for proportional risk (DDC) contributions from each return period, leading to a design that reduces extreme discrepancies across return periods. Furthermore, the intactness of the composite Pareto front during stress testing under low- to high-climate uplifts confirms the robustness of the design against increasingly intense rainstorms. These findings challenge the traditional urban flood risk management paradigm, which often relies on single maximum return period-driven designs. As BGI features are more frequently subjected to low- to moderate-intensity rainstorms, this study underscores the necessity of addressing large performance disparities during such events by incorporating a range of rainstorm return periods in general and shorter return periods specifically, within a multi-objective optimisation framework. Results indicate that while longer return periods still strongly influence composite BGI design, the proposed method simultaneously enforces considerable improvements for shorter return periods. Key parameters for developing robust composite BGI designs include selecting an appropriate risk objective function and range of rainstorm return periods. While incorporating more return periods can enhance design efficiency, computational constraints necessitate careful sampling, though not excessively limited, particularly when the risk objective function exhibits non-linear performance across return periods. By integrating five well-distributed return periods and designing a risk objective function that captures the full variability of BGI performance in risk reduction, this study advocates a paradigm shift in urban flood risk management from single maximum return period-based designs to robust, multi-return period-based designs.

Funding

The Natural Environmental Research Council (NERC) funded this research through the ONE Planet Doctoral Training Partnership (Grant: NE/S007512/1).

Conflict of interest

The authors declare no conflict of interest.

Appendix A: Supplementary information

Appendix B: Animation of the multi-return period-based BGI optimisation process

References

- Abduljaleel, Y., & Demissie, Y. (2021). Evaluation and Optimization of Low Impact Development Designs for Sustainable Stormwater Management in a Changing Climate. *Water*, *13*(20), 2889. <https://doi.org/10.3390/w13202889>
- Ahiablame, L. M., Engel, B. A., & Chaubey, I. (2012). Effectiveness of Low Impact Development Practices: Literature Review and Suggestions for Future Research. *Water, Air, & Soil Pollution*, *223*(7), 4253–4273. <https://doi.org/10.1007/s11270-012-1189-2>
- Alves, A., Gersonius, B., Kapelan, Z., Vojinovic, Z., & Sanchez, A. (2019). Assessing the Co-Benefits of green-blue-grey infrastructure for sustainable urban flood risk management. *Journal of Environmental Management*, *239*. <https://doi.org/10.1016/j.jenvman.2019.03.036>
- Alves, A., Gersonius, B., Sanchez, A., Vojinovic, Z., & Kapelan, Z. (2018). Multi-criteria Approach for Selection of Green and Grey Infrastructure to Reduce Flood Risk and Increase CO-benefits. *Water Resources Management*, *32*(7), 2505–2522. <https://doi.org/10.1007/s11269-018-1943-3>
- Bertsch, R., Glenis, V., & Kilsby, C. (2022). Building level flood exposure analysis using a hydrodynamic model. *Environmental Modelling & Software*, *156*, 105490. <https://doi.org/10.1016/j.envsoft.2022.105490>

- Bilskie, M. V., Angel, D. Del, Yoskowitz, D., & Hagen, S. C. (2022). Future Flood Risk Exacerbated by the Dynamic Impacts of Sea Level Rise Along the Northern Gulf of Mexico. *Earth's Future*, 10(4). <https://doi.org/10.1029/2021EF002414>
- Chan, S. C., Kendon, E. J., Fowler, H. J., Youngman, B. D., Dale, M., & Short, C. (2023). New extreme rainfall projections for improved climate resilience of urban drainage systems. *Climate Services*, 30, 100375. <https://doi.org/10.1016/j.cliser.2023.100375>
- D'Ambrosio, R., Balbo, A., Longobardi, A., & Rizzo, A. (2022). Re-think urban drainage following a SuDS retrofitting approach against urban flooding: A modelling investigation for an Italian case study. *Urban Forestry & Urban Greening*, 70, 127518. <https://doi.org/10.1016/j.ufug.2022.127518>
- Deb, K., & Jain, H. (2014). An Evolutionary Many-Objective Optimization Algorithm Using Reference-Point-Based Nondominated Sorting Approach, Part I: Solving Problems With Box Constraints. *IEEE Transactions on Evolutionary Computation*, 18(4), 577–601. <https://doi.org/10.1109/TEVC.2013.2281535>
- Deb, K., Pratap, A., Agarwal, S., & Meyarivan, T. (2002). A fast and elitist multiobjective genetic algorithm: NSGA-II. *IEEE Transactions on Evolutionary Computation*, 6(2), 182–197. <https://doi.org/10.1109/4235.996017>
- Environmental Agency. (2012). *The Tyneside Flood 28th June 2012: Hydrological Report*. EA Yorkshire & North East Region Hydrology Newcastle upon Tyne.
- Faulkner, D. (1999). Rainfall frequency estimation. In *Flood Estimation Handbook* (Vol. 2).
- Glenis, V., Kutija, V., & Kilsby, C. G. (2018). A fully hydrodynamic urban flood modelling system representing buildings, green space and interventions. *Environmental Modelling & Software*, 109, 272–292. <https://doi.org/10.1016/j.envsoft.2018.07.018>
- Gordon-Walker, S., Harle, T., & Naismith, I. (2007). *Cost-benefit of SUDS retrofit in urban areas*. Environment Agency.

- Iliadis, C., Glenis, V., & Kilsby, C. (2023). Representing buildings and urban features in hydrodynamic flood models. *Journal of Flood Risk Management*. <https://doi.org/10.1111/jfr3.12950>
- Iliadis, C., Glenis, V., & Kilsby, C. (2024). A cost-benefit ‘source-receptor’ framework for implementation of Blue-Green flood risk management. *Journal of Hydrology*, *634*, 131113. <https://doi.org/10.1016/j.jhydrol.2024.131113>
- Institute of Hydrology. (1975). Meteorological Studies. In *Flood Studies Report* (Vol. 2).
- Joshi, P., Leitão, J. P., Maurer, M., & Bach, P. M. (2021). Not all SuDS are created equal: Impact of different approaches on combined sewer overflows. *Water Research*, *191*, 116780. <https://doi.org/10.1016/j.watres.2020.116780>
- Kendon, E. J., Fischer, E. M., & Short, C. J. (2023). Variability conceals emerging trend in 100yr projections of UK local hourly rainfall extremes. *Nature Communications*, *14*(1), 1133. <https://doi.org/10.1038/s41467-023-36499-9>
- Liberalesso, T., Oliveira Cruz, C., Matos Silva, C., & Manso, M. (2020). Green infrastructure and public policies: An international review of green roofs and green walls incentives. *Land Use Policy*, *96*. <https://doi.org/10.1016/j.landusepol.2020.104693>
- Maier, H. R., Razavi, S., Kapelan, Z., Matott, L. S., Kasprzyk, J., & Tolson, B. A. (2019). Introductory overview: Optimization using evolutionary algorithms and other metaheuristics. *Environmental Modelling & Software*, *114*, 195–213. <https://doi.org/10.1016/j.envsoft.2018.11.018>
- Manchester City Council. (2021). *Manchester Green And Blue Infrastructure Strategy: Implementation Plan Refresh 2021-25*.
- Miller, J. D., & Hutchins, M. (2017). The impacts of urbanisation and climate change on urban flooding and urban water quality: A review of the evidence concerning the United Kingdom. *Journal of Hydrology: Regional Studies*, *12*, 345–362. <https://doi.org/10.1016/j.ejrh.2017.06.006>
- Newcastle City Council. (2016). *Local Flood Risk Management Plan*.

- O'Donnell, E., Thorne, C., Ahilan, S., Arthur, S., Birkinshaw, S., Butler, D., Dawson, D., Everett, G., Fenner, R., Glenis, V., Kapetas, L., Kilsby, C., Krivtsov, V., Lamond, J., Maskrey, S., O'Donnell, G., Potter, K., Vercruyssen, K., Vilcan, T., & Wright, N. (2020). The blue-green path to urban flood resilience. *Blue-Green Systems*, 2(1), 28–45. <https://doi.org/10.2166/bgs.2019.199>
- Penning-Rowsell, E., Priest, S., Parker, D., Morris, J., Tunstall, S., Viavattene, C., Chatterton, J., & Owen, D. (2014). *Flood and coastal erosion risk management: a manual for economic appraisal*. Routledge.
- Qin, H., Li, Z., & Fu, G. (2013). The effects of low impact development on urban flooding under different rainfall characteristics. *Journal of Environmental Management*, 129, 577–585. <https://doi.org/10.1016/j.jenvman.2013.08.026>
- Rentschler, J., Avner, P., Marconcini, M., Su, R., Strano, E., Voudoukas, M., & Hallegatte, S. (2023). Global evidence of rapid urban growth in flood zones since 1985. *Nature*, 622(7981). <https://doi.org/10.1038/s41586-023-06468-9>
- Robinson, A., Lehmann, J., Barriopedro, D., Rahmstorf, S., & Coumou, D. (2021). Increasing heat and rainfall extremes now far outside the historical climate. *Npj Climate and Atmospheric Science*, 4(1), 45. <https://doi.org/10.1038/s41612-021-00202-w>
- Rodriguez, M., Fu, G., Butler, D., Yuan, Z., & Sharma, K. (2021). Exploring the spatial impact of green infrastructure on urban drainage resilience. *Water (Switzerland)*, 13(13), 1–21. <https://doi.org/10.3390/w13131789>
- Rosenbloom, J. (2018). Fifty shades of gray infrastructure: Land use and the failure to create resilient cities. *Wash. L. Rev.*, 93, 317.
- Rossman, L. A., & others. (2010). *Storm water management model user's manual, version 5.0*. National Risk Management Research Laboratory, Office of Research and~....
- Salhab, M., & Rentschler, J. (2020). People in Harm's Way: Flood Exposure and Poverty in 189 Countries. In *People in Harm's Way: Flood Exposure and Poverty in 189 Countries*. <https://doi.org/10.1596/1813-9450-9447>

Salinas-Rodriguez, C., Gersonius, B., Zevenbergen, C., Serrano, D., & Ashley, R. (2018). A Semi Risk-Based Approach for Managing Urban Drainage Systems under Extreme Rainfall. *Water*, *10*(4), 384. <https://doi.org/10.3390/w10040384>

Scottish-Government. (2018). Appendix 5 Example of estimating flood risk damages to properties. In *Surface water management planning guidance* (pp. 98–101). <https://www.gov.scot/publications/flood-risk-management-scotland-act-2009-surface-water-management-planning/pages/16/>

Seyedashraf, O., Bottacin-Busolin, A., & Harou, J. J. (2021). A Disaggregation-Emulation Approach for Optimization of Large Urban Drainage Systems. *Water Resources Research*, *57*(8). <https://doi.org/10.1029/2020WR029098>

Sharma, S., Lee, B. S., Nicholas, R. E., & Keller, K. (2021). A Safety Factor Approach to Designing Urban Infrastructure for Dynamic Conditions. *Earth's Future*, *9*(12). <https://doi.org/10.1029/2021EF002118>

Ur Rehman, A., Glenis, V., Lewis, E., & Kilsby, C. (2024). Multi-objective optimisation framework for Blue-Green Infrastructure placement using detailed flood model. *Journal of Hydrology*, *638*, 131571. <https://doi.org/10.1016/j.jhydrol.2024.131571>

Venter, G. (2010). Review of Optimization Techniques. In *Encyclopedia of Aerospace Engineering*. <https://doi.org/10.1002/9780470686652.eae495>

Vercruyse, K., Dawson, D. A., Glenis, V., Bertsch, R., Wright, N., & Kilsby, C. (2019). Developing spatial prioritization criteria for integrated urban flood management based on a source-to-impact flood analysis. *Journal of Hydrology*, *578*, 124038. <https://doi.org/10.1016/j.jhydrol.2019.124038>

Wang, J., Liu, J., Mei, C., Wang, H., & Lu, J. (2022). A multi-objective optimization model for synergistic effect analysis of integrated green-gray-blue drainage system in urban inundation control. *Journal of Hydrology*, *609*, 127725. <https://doi.org/10.1016/j.jhydrol.2022.127725>

- Ward, P. J., de Moel, H., & Aerts, J. C. J. H. (2011). How are flood risk estimates affected by the choice of return-periods? *Natural Hazards and Earth System Sciences*, 11(12), 3181–3195. <https://doi.org/10.5194/nhess-11-3181-2011>
- Webber, J. L., Fletcher, T. D., Cunningham, L., Fu, G., Butler, D., & Burns, M. J. (2020). Is green infrastructure a viable strategy for managing urban surface water flooding? *Urban Water Journal*, 17(7), 598–608. <https://doi.org/10.1080/1573062X.2019.1700286>
- Wheeler, A. F. (2016). Newcastle city strategic surface water management plan. *Final Report*. See [https://www. Newcastle. Gov. Uk/Sites/Default/Files/Wwwfileroot/Planning-and-Buildings/Planning-Policy/Newcastle_city_strategic_surface_water_management_plan_jan_2016. Pdf](https://www.newcastle.gov.uk/sites/default/files/wwfileroot/Planning-and-Buildings/Planning-Policy/Newcastle_city_strategic_surface_water_management_plan_jan_2016.pdf) (Accessed 22 May 2024).
- Zhi, X., Xiao, Y., Chen, L., Hou, X., Yu, Y., Zhou, X., Fu, Y., Chen, B., & Shen, Z. (2022). Integrating cost-effectiveness optimization and robustness analysis for low impact development practices design. *Resources, Conservation and Recycling*, 185, 106491. <https://doi.org/10.1016/j.resconrec.2022.106491>